

PHYSICS

Atomic mapping of periodic dipole waves in ferroelectric oxide

Feng-Hui Gong^{1,2†}, Yun-Long Tang^{1†}, Yin-Lian Zhu^{1,3*}, Heng Zhang^{1,2}, Yu-Jia Wang¹, Yu-Ting Chen^{1,2}, Yan-Peng Feng^{3,4}, Min-Jie Zou^{3,4}, Bo Wu³, Wan-Rong Geng^{3,4}, Yi Cao^{1,2}, Xiu-Liang Ma^{1,5*}

A dipole wave is composed of head-to-tail connected electric dipoles in the form of sine function. Potential applications in information carrying, transporting, and processing are expected, and logic circuits based on nonlinear wave interaction are promising for dipole waves. Although similar spin waves are well known in ferromagnetic materials for their roles in some physical essence, electric dipole wave behavior and even its existence in ferroelectric materials are still elusive. Here, we observe the atomic morphology of large-scale dipole waves in PbTiO₃/SrTiO₃ superlattice mediated by tensile epitaxial strains on scandate substrates. The dipole waves can be expressed in the formula of $y = A \sin(2\pi x/L) + y_0$, where the wave amplitude (A) and wavelength (L) correspond to 1.5 and 6.6 nm, respectively. This study suggests that by engineering strain at the nanoscale, it should be possible to fabricate unknown polar textures, which could facilitate the development of nanoscale ferroelectric devices.

INTRODUCTION

A ferroelectric features an asymmetry in charge that is switchable by an applied electric field. Likewise, a ferromagnet has an asymmetry in spin that can be reoriented by an external magnetic field (1). Despite the fundamental differences between ferroelectrics and ferromagnets, the topological domains in these two ferroic materials are quite analogous. With the recent development of aberration-corrected transmission electron microscopy (TEM), the topological domains that are well known in ferromagnets have been directly visualized at the atomic scale in ferroelectrics, such as flux closures (2, 3), vortices (4–7), skyrmions (8), center-type domains (9, 10), and merons (11).

In the studies of relationship between low temperature-specific heat (C_v) and temperature (T) in ferromagnetic materials, a classic equation of $C_v = \alpha T^{3/2} + \beta T^3$ was established (12–15), where the term of $T^{3/2}$ is known to result from the contribution of spin wave. Experimentally, more and more investigations indicate that the above equation is also suitable for ferroelectric materials (16–23). Nevertheless, the physical insight of the term $T^{3/2}$ for ferroelectric materials is not clarified, although, theoretically, Gonzalo *et al.* (24–26) applied a spin wave-like dispersion relation model and proposed that the term of $T^{3/2}$ might be associated with electric dipole waves.

The spin waves in ferromagnetic materials are thus well understood, but similar electric dipole wave behavior and even its existence in ferroelectrics are unclear so far. Although electric dipole waves are theoretically explored in low-temperature ultrathin lead-zirconate-titanate

films (27), direct observations only show a transition state under electric fields (28, 29) or locally occur in an irregular manner in ferroelectric films (30).

In this study, we have grown PbTiO₃/SrTiO₃ (PTO/STO) superlattices under variant tensile strains (fig. S1) by using pulsed laser deposition (PLD). After the deposition, the as-grown superlattice films were quenched rapidly by lifting the heating coil. Using aberration-corrected high-angle annular dark-field (HAADF) Z-contrast scanning TEM (STEM) imaging, we visualize, at the atomic scale, the existence of periodic electric dipole waves, which is further rationalized by phase-field simulations.

RESULTS AND DISCUSSION

Generally, PTO is paraelectric and has a simple cubic crystal structure above Curie temperature ($T_c \sim 765$ K), which is governed by short-range repulsions. It undergoes paraelectric-ferroelectric phase transition and becomes a polar tetragonal lattice determined by long-range Coulomb forces (Fig. 1A) below T_c . The tetragonal PTO unit cell involves considerable displacements of Pb²⁺ and Ti⁴⁺ cations relative to O²⁻ anions, leading to a separation of the positive and negative charge centers in each unit cell, and thus, an electric dipole forms. A projected atomic configurations and spontaneous polarization (P_s) are marked in Fig. 1 (B and C), respectively. The shifts of Ti⁴⁺ (δ_{Ti}) can be used to determine the polarizations of PTO unit cells, whose direction is opposite to P_s (Fig. 1C).

A low-magnification cross-sectional HAADF-STEM image of the tensile strained PTO/STO superlattice grown on GdScO₃ (001)pc (where “pc” refers to “pseudo-cubic”, detailed in table S1) substrate confirms that all the PTO/STO and the PTO/GdScO₃ interfaces are sharp and coherent (Fig. 1D). Note that periodically arranged, subtle darker and brighter contrast exists in each PTO layer, suggesting that possible polar structures may emerge regularly in these PTO layers. To get a more general glance of the quality of the PTO/STO superlattice, film scale symmetric Bragg scans (Fig. 1E) were performed, where the smooth surface and the high quality of superlattice are further confirmed.

¹Shenyang National Laboratory for Materials Science, Institute of Metal Research, Chinese Academy of Sciences, Wenhua Road 72, Shenyang 110016, China. ²School of Materials Science and Engineering, University of Science and Technology of China, Wenhua Road 72, Shenyang 110016, China. ³Songshan Lake Materials Laboratory, Dongguan 523808, Guangdong, China. ⁴Institute of Physics, Chinese Academy of Sciences, Beijing 100190, China. ⁵State Key Lab of Advanced Processing and Recycling on Non-ferrous Metals, Lanzhou University of Technology, Langongping Road 287, Lanzhou 730050, China.

*Corresponding author. Email: ylzhu@imr.ac.cn (Y.-L.Z.); xliu@imr.ac.cn (X.-L.M.)

†These authors contributed equally to this work.

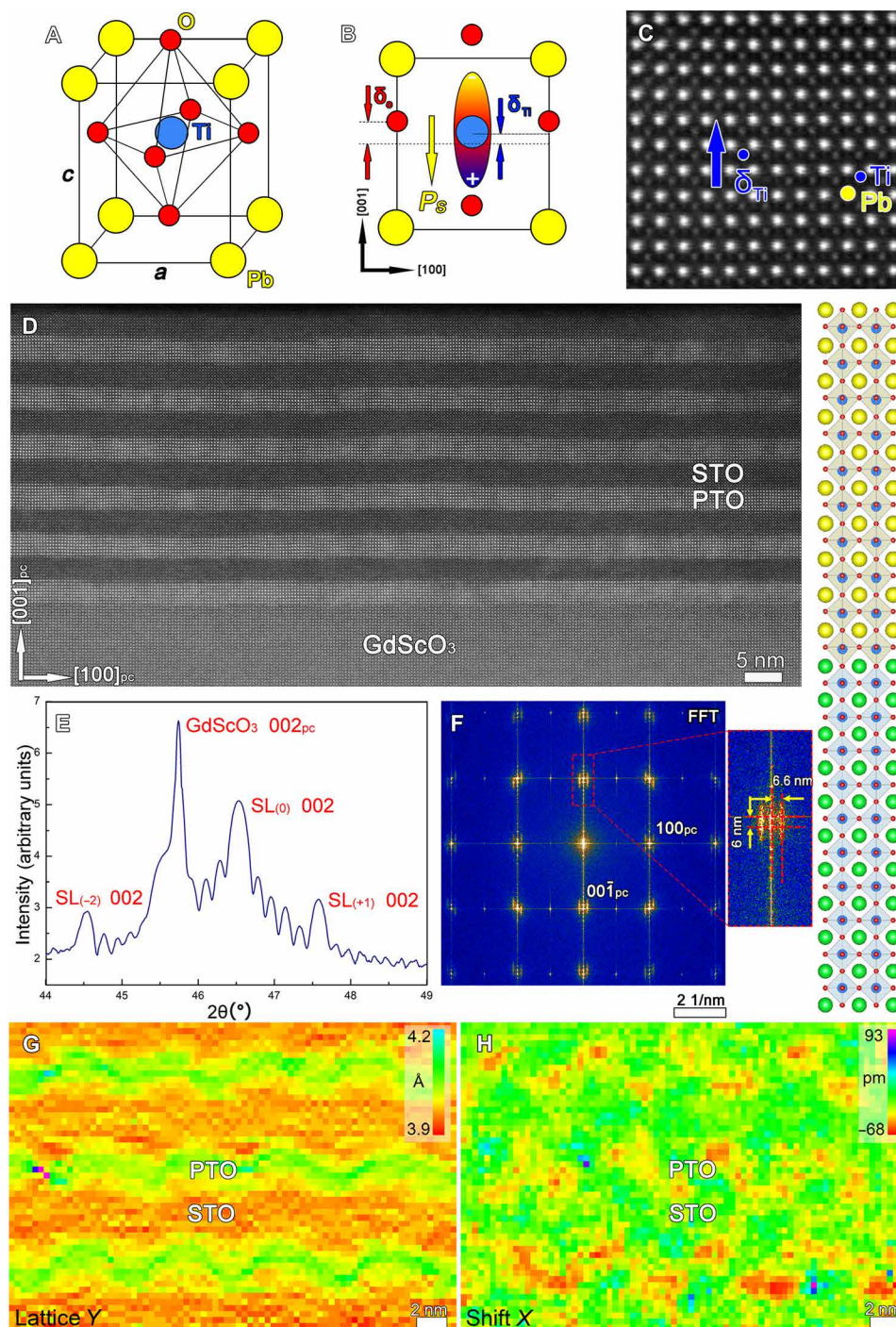


Fig. 1. Structural characterization of $[(\text{PbTiO}_3)_7/(\text{SrTiO}_3)_7]_6$ superlattices. (A) Schematic of unit cell of tetragonal PTO (yellow, Pb; blue, Ti; and red, O). (B) Projection of the unit cell along the $[010]$ direction. The displacement of Ti^{4+} is marked by δ_{Ti} , and the displacement of O^{2-} is marked by δ_{O} . (C) HAADF-STEM image of the PTO/STO superlattices along the $[010]_{\text{pc}}$. (D) Low-magnification STEM image of the PTO/STO superlattices, together with a schematic illustration of the superlattices structure (green, Sr; gray- and cyan-shaded regions surrounding Ti atoms show oxygen octahedra). (E) High-resolution θ - 2θ symmetric scan of the PTO/STO superlattices showing the presence of Pendellösung fringes. (F) The fast Fourier transform (FFT) pattern for (D). (G and H) Out-of-plane lattice spacing map and shift X extracted from HAADF-STEM images, respectively.

A hidden periodic structure is revealed by the fast Fourier transform (FFT; Fig. 1F) pattern of Fig. 1D. Here, the period of this structure is ~ 6.6 nm along the in-plane direction, and the thickness of a single PTO/STO superlattice period is about ~ 6 nm. Further,

lattice Y extracted from an atomic scale-resolved HAADF-STEM image (fig. S2) is shown in Fig. 1G, where a wave-like, hidden periodic structure can be identified (detailed in Materials and Methods). Unit cells with larger lattice Y (in green) in PTO layers form

periodic sinusoidal wave-shaped arrays here. The shift X (in-plane component of δ_{Ti}) shown in Fig. 1H also displays a sinusoidal wave shape like that of the lattice Y (details for extracting the lattice and δ_{Ti} can be found in Materials and Methods). It should be emphasized here that the maximum values of shift X just appear at the peaks and valleys of the wave-shaped distributions, which is also a feature of wave-like polar structure. These details imply that a possible periodic polar structure should exist in these PTO layers.

To reveal the polar structures in the PTO layers here, two-dimensional (2D) δ_{Ti} -based polar mapping analysis is performed for the atomically resolved HAADF-STEM images (Fig. 2). One PTO layer with two adjacent STO layers is displayed in Fig. 2A. The positions of Pb^{2+} and Ti^{4+} columns are depicted by yellow and blue circles, respectively. Directions of polarizations determined by $-\delta_{\text{Ti}}$ are indicated by yellow arrows. It is seen that the polarizations rotate continuously and feature periodically from right to upper right, right, lower right, and then back to right again, forming a perfect periodic wave. In addition, nearly zero polarization outside the wave line is observed, and there is no obvious domain wall. All the above results suggest that an electric dipole wave is formed throughout the PTO layer.

More general details are revealed for this PTO/STO superlattice to further confirm the dipole wave and possible wave arrays. Polar mapping for the larger area HAADF-STEM image (fig. S2) reveals not only the existence of such polar waves but also the formation of arrays of this electric dipole wave (Fig. 2B, in blue). The neglectable Ti^{4+} displacement in the STO layer indicates the effectiveness and reliability of the polar mappings. The out-of-plane period of the

superlattice and in-plane period of the electric dipole waves obtained by Fig. 2B are consistent with the FFT pattern (Fig. 1F), which indicates that the in-plane modulation displayed in Fig. 1F is a kind of periodic polar structure. Further, enlarged polar mappings for the green and red boxed areas (Fig. 2, C and D) reveal continuous polarization rotation at the peak and valley areas, indicating the existence of such electric dipole waves (as schematized in Fig. 2E). We have further applied annular bright field (ABF) imaging, which is more sensitive for recording O atom columns (Fig. 3A; the direct ABF-STEM image corresponding to Fig. 3A was shown in fig. S3). Corresponding superposition of δ_{Ti} and δ_{O} vector maps with the experimental image (Fig. 3, B and C) reveal electric dipole waves, which are consistent with the HAADF images (Fig. 2).

In addition, quantitative statistical analysis corroborates periodic order parameter variation in these polar structures, which is consistent with the wave characteristic in these electric dipole waves (Fig. 4). Figure 4A shows the polarization mapping of electric dipole wave in the first PTO layer (Fig. 2B). First, we have extracted the out-of-plane component of δ_{Ti} for all the seven layers of PTO unit cells (circles in Fig. 4B and fig. S4). Clear periodic characters like sinusoidal distributions can be identified. To get further insight of the δ_{Ti} distributions, we have fitted these Ti^{4+} displacements in each PTO layer (black curves in Fig. 4B and fig. S4). Here, the sinusoidal function equation fitted for the center layer of PTO unit cells (fourth layer of the PTO unit cells, yellow solid box labeled 4 in Fig. 4A) is $y = 25.44 \cdot \sin[2\pi(x - 0.91)/6.64] + 0.64$, where the wave amplitude and wavelength are 25.44 pm and 6.64 nm, respectively (detailed in the Supplementary Materials). More generally, it is

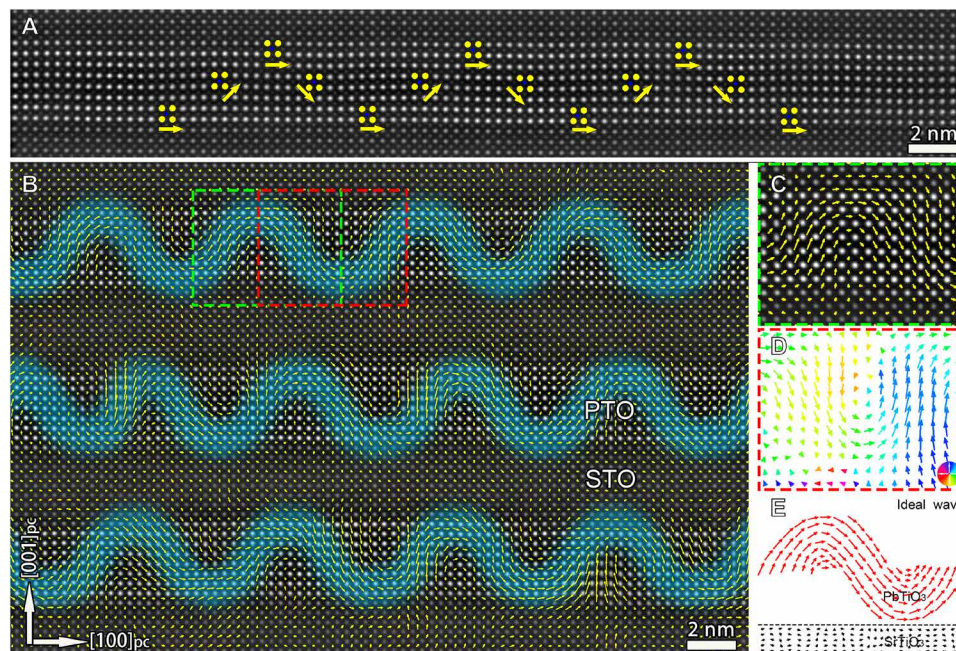


Fig. 2. Superposition of atomically resolved HAADF-STEM images and Ti^{4+} displacement vector maps showing the periodic array of electric dipole waves.

(A) Atomically resolved HAADF-STEM image corresponding to the areas of several wavelengths of electric dipole waves. The yellow and blue circles denote the position of Pb^{2+} and Ti^{4+} columns, respectively. (B) Cross-sectional HAADF-STEM image with a superposition of the polar displacement vectors (\mathbf{P} , indicated by yellow arrows) for the PTO/STO superlattices, showing that periodic array of electric dipole waves present in each PTO layer. (C) A magnified image of one peak of electric dipole waves from the green dotted box area in (B) showing the full density of data points for each atom and the continuous rotation of the polarization state within such electric dipole waves. (D) A magnified image of a single valley of electric dipole waves from the red dotted box area in (B). The colors of arrows indicate angles between the direction of polarization and the horizontal direction. (E) Schematic of one cycle of electric dipole waves.

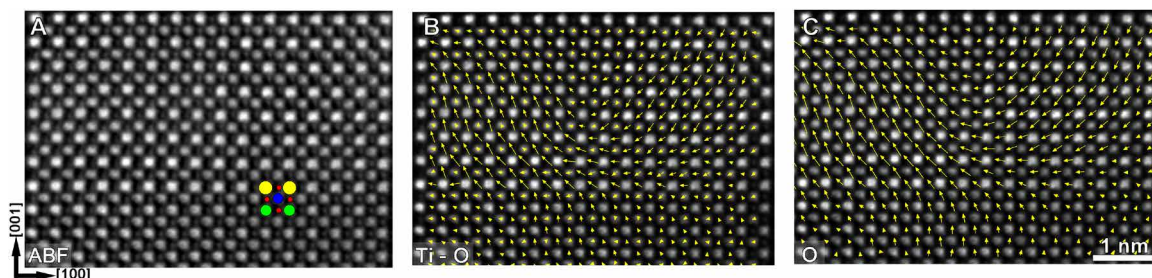


Fig. 3. ABF imaging of the dipole wave. (A) An annular bright field (ABF)-STEM image of the PTO/STO superlattice grown on NdScO₃ substrate (red circle, O atom column). Here, the image contrast was inverted to ease visual inspection. (B) Superposition of the reversed δ_{Ti} and δ_O vectors with the experimental image (A). (C) Superposition of the reversed δ_O vectors with the experimental image (A).

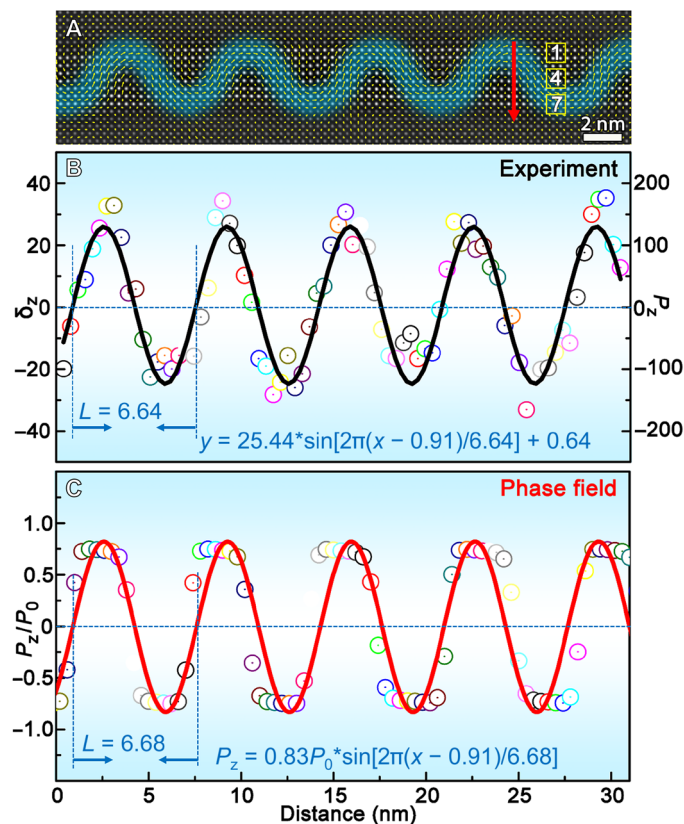


Fig. 4. Sinusoidal polar distributions extracted from the periodic array of electric dipole waves. (A) Periodic electric dipole wave in one PTO layer between two adjacent STO layers from Fig. 2B. According to the direction of the red arrow, the unit cells in one PTO layer are divided into seven independent layers, as shown by the Arabic numbers 1 to 7 in the yellow solid line boxes. (B) Ion displacement (δ_z , pm) and polarization value (P_z , $\mu\text{C}/\text{cm}^2$) in out-of-plane direction as a function of horizontal distance and corresponding sinusoidal function fitting. The sinusoidal relationship of the polar structures here can be seen clearly in the fourth unit cell layer. (C) The P_z component of polarization in the middle unit cell layer of a PTO layer and the sinusoidal fitting equation calculated from phase-field simulations.

found that the sinusoidal function of each PTO layer of unit cells can be described as the same equation as $y = A \cdot \sin[2\pi(x - \Delta)/L] + y_0$, where A is the wave amplitude and L is the wavelength (Fig. 4 and fig. S4). The wavelength of wave for all PTO unit cell layers is almost constant (~ 6.6 nm).

We have performed phase-field simulations to understand the effect of superlattice periods and epitaxial strains on the formation of electric dipole waves. The phase-field model of $(\text{PTO})_n/(\text{STO})_n$ (n represents the superlattice period) contains two PTO layers and two STO layers that are alternatively arranged on corresponding substrates (detailed in Materials and Methods).

A series of polar wave models with different periods were constructed in phase-field simulations. The calculated total energy density versus the period for $(\text{PTO})_9/(\text{STO})_9$ at $\epsilon = 1.3\%$ is shown in fig. S5. In the fitting curve, it is found that the optimal period is about 7 nm. Figure 4C shows the P_z component in the lower PTO layer of the model with the lowest total energy density. The data are also fitted using the same sinusoidal function as Fig. 4B, and the fitting result is $P_z = 0.83P_0 \cdot \sin[2\pi(x - 0.91)/6.68]$, in which the polarization amplitude is $0.83P_0$ ($P_0 = 75.7 \mu\text{C}/\text{cm}^2$), and the wavelength is 6.68 nm (red curves in Fig. 4C). These results are well consistent with the experimental observation. Thus, the wave characteristic of these polar structures is established.

To explore the universality of electric dipole waves and confirm that rapid quenching is a suitable condition for stabilizing these polar structures, we have further grown PTO/STO superlattices on DyScO₃, SmScO₃, and NdScO₃ substrates (lattice mismatches with PTO are 1.36, 2.15, and 2.64%, calculation method is shown in table S2) using the same conditions as the superlattice grown on GdScO₃. Diffraction contrast images show that there are similar large-scale periodic structures in all of these superlattices (fig. S6). Polarization mappings (Fig. 5, A to D) corresponding to their high-resolution HAADF-STEM images (fig. S7) indicate that these periodic polar structures are the electric dipole waves, which are stabilized at room temperature by quenching. In particular, by comparing the mappings in Fig. 5 (A to D), it is found that there is a negligible change in the periods of these electric dipole waves under different strain conditions. In addition, the electric dipole waves are all stabilized in the form of arrays (figs. S8 to S11) rather than in a single layer of PTO, which further confirms the generality of these electric dipole wave structures.

A typical polarization map based on the phase-field simulation of $(\text{PTO})_n/(\text{STO})_n$ at the strain state of $\sim 1.5\%$ with $n = 10$ is shown in Fig. 5E. The continuous polarization rotation of the electric dipole waves is highlighted by the green solid line, which is in good agreement with the experimental results. To understand the effect of superlattice period and epitaxial strain on the formation of electric dipole waves, the strain-thickness phase diagram is constructed, as shown in Fig. 5F. Various phase regions are marked by different symbols and colors. We chose the simulation results on the DyScO₃ substrate (average strain, $\approx 1.28\%$, labeled by a red arrow in Fig. 5F)

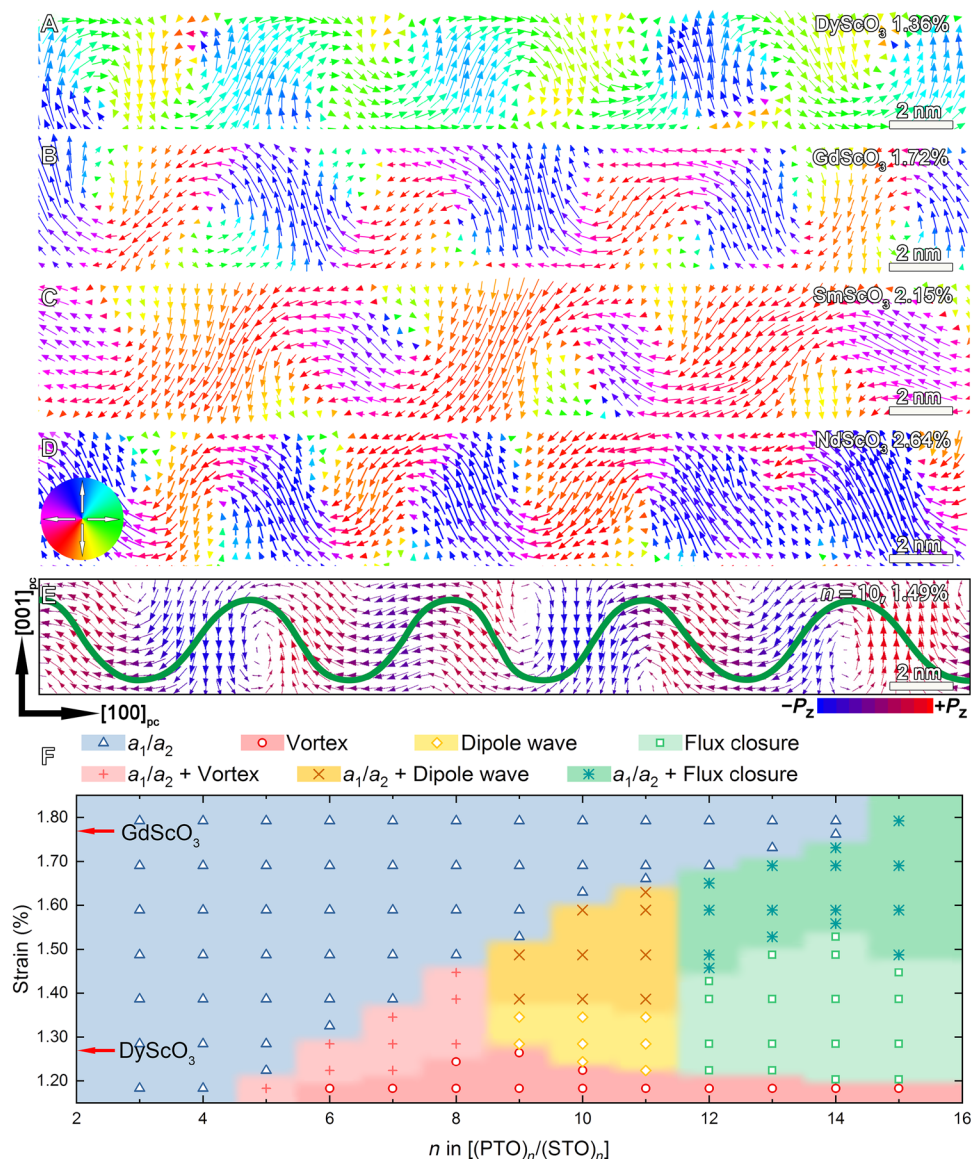


Fig. 5. Electric dipole waves under different tensile strain conditions and strain-period phase diagram of (PTO)_n/(STO)_n superlattice obtained by phase-field simulations. (A to D) Electric dipole waves in PTO/STO superlattices grown the DyScO₃, GdScO₃, SmScO₃, and NdScO₃ orthogonal substrates under different tensile strain conditions (1.36, 1.72, 2.15, and 2.64%). The colors of the arrows show angles between the direction of polarization and the horizontal direction. (E) The polarization distribution of a PTO layer at medium period ($n = 10$) at the strain state of $\sim 1.5\%$, as predicted by phase-field simulations. The ordered electric dipole wave arrays are highlighted by the green solid line. (F) Phase diagram of (PTO)_n/(STO)_n superlattice as a function of superlattice period n and substrate strain, obtained from phase-field simulations. The strain positions of scandate substrate are labeled by red arrows.

to show the evolution of domain structure with the superlattice period, because the four phase regions on this substrate cover all representative domain structures. Typical a_1/a_2 domains are energetically favorable at small period ($n \leq 5$), as shown in fig. S12 (a and b). With increasing periods from $n = 6$ to $n = 8$, the coexisting phase of a_1/a_2 and vortex is predicted, in which tube-like vortex arrays interweave with a_1/a_2 domains are shown in fig. S12 (c and d). After reaching a critical period, the domain structure evolves from the vortex ($n = 9$) to the electric dipole wave ($n = 10 \sim 11$). The 3D structure of electric dipole waves in fig. S12e shows periodic long stripes along the $[010]_{pc}$ direction and wave-like continuous polarization rotation along the $[100]_{pc}$ direction (fig. S12f), which is

consistent with the experimental result. Last, the electric dipole wave transforms to flux-closure domains at larger period ($n \geq 12$; fig. S12, g and h). For the GdScO₃ substrate, the strain state (average strain $\approx 1.77\%$, labeled by a red arrow in Fig. 5F) is very close to the phase region of mixed a_1/a_2 domains and electric dipole waves. Considering that the domain structures obtained by quenching in experiment are possibly metastable, it is thus reasonable to observe electric dipole waves in films grown on this substrate. For the SmScO₃ and NdScO₃ cases, the strain in these superlattice films can be partially released by the interface dislocations, which may allow the emergence of the electric dipole waves. Figure 6 shows the polarization vector maps of (PTO)₁₀/(STO)₁₀ at different strain states. Here,

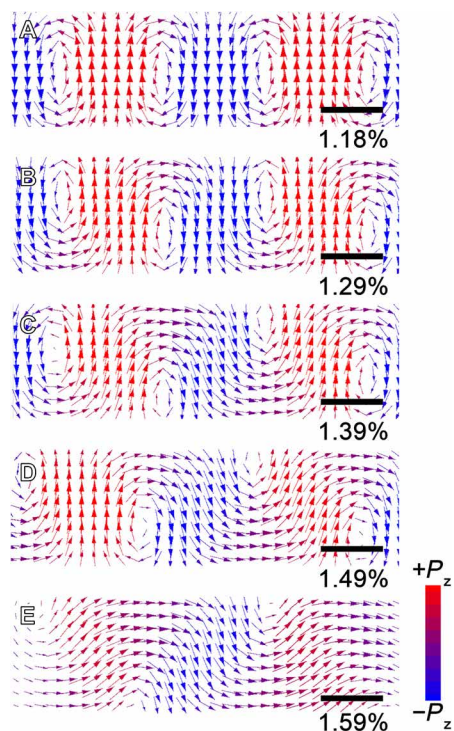


Fig. 6. The evolution of polar structures in PTO layers of the (PTO)₁₀/(STO)₁₀ superlattice versus strains by phase-field simulations. Tensile strains will promote wave-like polarization configurations, as can be seen from (A) to (E). Scale bars, 5 nm.

it is clear that as the substrate strain increases, vortices evolve into waves and the wave-like polarization configurations become more and more obvious, which may indicate that larger tensile strains are more suitable for the formation of electric dipole waves.

The conditions of stabilizing such electric dipole wave arrays at room temperature and the reason why thermodynamics-based quenching treatment has a substantial effect on these polarization states are of interest. Compared with thermodynamic equilibrium, nonequilibrium kinetic plays an important role in stabilizing some metastable states. For example, fast cooling treatment can create charged domain walls in ferroelectric films (31), which are generally unstable because of their high free energy. In addition, ultrafast laser can stabilize supercrystal phase converted by common ferroelectric superlattice (32), which is generally inaccessible. As a comparison, the (PTO₇/STO₇)₆ superlattice without quenching shows the polar vortex array as observed previously (fig. S13) (4). Our results show that the nonequilibrium quenching, in addition to the external tensile strains rationalized by the phase-field simulations, may also help to stabilize the room-temperature periodic dipole waves (figs. S8 to S11) in ferroelectric superlattices.

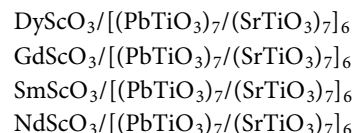
Our results indicate that the periodic array of electric dipole waves can be artificially stabilized by engineering strains. The dipole wave is universal at room temperature in the ferroelectric oxide, which is analogous to the spin wave in ferromagnetic materials. The strategy that is based on dynamic nonequilibrium process expands the research ideas in the field of ferroelectricity, which might create more previously unknown phenomena. The present study provides a physical spectrum of electric dipole waves, which may contribute to further theoretical and dynamic explorations on the

topological structures in ferroelectric thin films. The controlled growth of electric dipole waves realizes a great step toward the development of ferroelectric nanoscale devices.

MATERIALS AND METHODS

Materials

We have grown a series of superlattices samples under different tensile strain conditions



The main experiments were completed using PTO/STO superlattice samples deposited on GdScO₃ substrates in Fig. 1, 2, and 4. These rare-earth scandates have an orthorhombic structure, which can be analyzed as a pseudo-cubic structure. Table S1 shows the corresponding crystallographic orientation between orthogonal and pseudo-cubic structure. These substrates cause superlattices to be subjected to different tensile strains.

Methods

Superlattices growth using PLD

The superlattice were deposited on DyScO₃(110), GdScO₃(110), SmScO₃(110), and NdScO₃(110) orthorhombic substrates using the Coherent COMPex Pro 201 F KrF excimer laser with $\lambda = 248$ nm. The orthogonal substrate was ultrasonically cleaned in acetone. The PTO target is 3 mole percent of Pb-enriched sintered ceramics. The STO target is sintered ceramics with standard stoichiometric ratio. Before deposition, the charge and discharge process was repeated three times to make the gas pure and even in the cavity. Substrates were heated up to 750°C holding for 5 min to clean the surface of substrate and then kept at 700°C to grow superlattices. During the process of growing the PTO/STO superlattices, laser energy of 370 mJ, oxygen pressure of 75 mtorr, and a repetition rate of 4 Hz were used. Following the growth process, an annealing at 700°C in an oxygen pressure of 200 torr for 5 min was performed. Then, the heating coil was lifted quickly to be apart from the substrate for quenching, which is for rapid cooling resulting in dynamic nonequilibrium.

Symmetric X-ray diffraction scans

A PANalytical X'Pert Pro x-ray diffractometer with a copper source was used to characterize the superlattice. Symmetric x-ray diffraction scan with appropriate angle range was adopted to reveal the structural order in the out-of-plane direction. The x-ray wavelength from the copper source was 1.54059 Å.

TEM and aberration-corrected STEM characterization

Cross-sectional samples for the TEM and STEM observations were prepared by slicing, grinding, dimpling, and, finally, ion milling by using Gatan Precision Ion Polishing System 691 and 695. In the initial stage of ion milling, the voltage was set to 5 kV, and the ion beam incident angle was 8°. The voltage and incident angle were gradually reduced to 3.5 kV and 5°, respectively, taking 10 min as a step until the appearance of colored stripes. The final ion-milling voltage was 0.5 kV (691) and 0.1 kV (695) to reduce amorphous layer causing by ion-beam damage. Diffraction contrast TEM images and selected area electron diffraction patterns were acquired by using a Tecnai G² F30 transmission electron microscope (FEI).

HAADF-STEM images were obtained using a Titan G² 60-300 microscope with a high-brightness field-emission gun and double aberration (Cs) correctors from CEOS working at 300 kV. The resolution of the STEM is 0.8 Å. Each of the HAADF-STEM images is obtained by superimposing 20 original images collected in a very short period of time from the same area. The purpose is to reduce the influence of scanning noise and random sample drift. This operation is achieved by Velox software (FEI). This process facilitates the study of the complex polar structures involving electric dipole wave in the present study. All atomic-scale HAADF-STEM images have been drift corrected and filtered.

Peak finding

All HAADF-STEM images in the paper were processed by center-circle filtering and adjusting brightness and contrast. We already know that the intensity of the atomic column is proportional to the square of the atomic number. The Pb²⁺ columns appear as the brightest dots comparing to the brightness of Ti⁴⁺ columns in the HAADF-STEM images. To determine the direction of Ti⁴⁺ displacement and the direction of polarization, the position of each atomic column was extracted by 2D Gaussian fitting using MATLAB software. The direction of Ti⁴⁺ displacement (δ_{Ti}) was calculated by confirming the center of the four nearest Pb²⁺ neighbors. The direction of \mathbf{P}_s is opposite to the δ_{Ti} vectors. In addition, it can obtain ion displacement and lattice constant. The polarization was determined by fitting atom column positions as Gaussian peaks using MATLAB software (33). The polarization value (\mathbf{P}_s) has a linear relationship with the displacement of the Ti⁴⁺ (δ_{Ti}). The calculation of the polarization value in Fig. 4B is completed (34). The calculation formula of the \mathbf{P}_s is as follows

$$\mathbf{P}_s = 1.96k\delta_{\text{Ti}} \quad (1)$$

where \mathbf{P}_s ($\mu\text{C}/\text{cm}^2$) is the calculated spontaneous polarization value of ferroelectric PTO. For ferroelectric PTO, the value of k is approximately 2726 ($\mu\text{C}/\text{cm}^2$)/nm. δ_{Ti} (nm) is the displacement value of Ti⁴⁺.

Phase-field simulations

The 3D phase-field simulations were performed to simulate the domain structures of (PbTiO₃)_{*n*}/(SrTiO₃)_{*n*} superlattice as a function of superlattice period n and substrate strain. The order parameters are chosen as the three components of polarization vectors. The total energy density of the system contains contributions from the bulk, gradient, elastic, and electric energy densities

$$f = f_{\text{bulk}}(P_i) + f_{\text{grad}}(P_{i,j}) + f_{\text{elas}}(P_i, \epsilon_{kl}) + f_{\text{ele}}(P_i, E_i) \quad (2)$$

The first term is the bulk energy density

$$\begin{aligned} f_{\text{bulk}} = & \alpha_1(P_1^2 + P_2^2 + P_3^2) + \alpha_{11}(P_1^4 + P_2^4 + P_3^4) \\ & + \alpha_{12}(P_1^2P_2^2 + P_2^2P_3^2 + P_1^2P_3^2) + \alpha_{111}(P_1^6 + P_2^6 + P_3^6) \\ & + \alpha_{112}[P_1^4(P_2^2 + P_3^2) + P_2^4(P_1^2 + P_3^2) + P_3^4(P_1^2 + P_2^2)] + \alpha_{123}P_1^2P_2^2P_3^2 \end{aligned} \quad (3)$$

The second term is the gradient energy density

$$\begin{aligned} f_{\text{grad}} = & \frac{1}{2}G_{11}(P_{1,1}^2 + P_{2,2}^2 + P_{3,3}^2) + G_{12}(P_{1,1}P_{2,2} + P_{2,2}P_{3,3} + P_{1,1}P_{3,3}) \\ & + \frac{1}{2}G_{44}[(P_{1,2} + P_{2,1})^2 + (P_{2,3} + P_{3,2})^2 + (P_{3,1} + P_{2,1})^2] \end{aligned} \quad (4)$$

The third term is the elastic energy density

$$f_{\text{elas}} = \frac{1}{2}C_{ijkl}(\epsilon_{ij} - \epsilon_{ij}^0)(\epsilon_{kl} - \epsilon_{kl}^0) \quad (5)$$

where ϵ_{ij} is the total strain and ϵ_{ij}^0 is the spontaneous strain. Their difference is the elastic strain. The spontaneous strain is related to the polarization by the electrostrictive coefficients

$$\begin{aligned} \epsilon_{11}^0 &= Q_{11}P_1^2 + Q_{12}(P_2^2 + P_3^2) \\ \epsilon_{22}^0 &= Q_{11}P_2^2 + Q_{12}(P_1^2 + P_3^2) \\ \epsilon_{33}^0 &= Q_{11}P_3^2 + Q_{12}(P_1^2 + P_2^2) \\ \epsilon_{23}^0 &= Q_{44}P_2P_3 \\ \epsilon_{13}^0 &= Q_{44}P_1P_3 \\ \epsilon_{12}^0 &= Q_{44}P_1P_2 \end{aligned} \quad (6)$$

The last term is the electric energy density

$$f_{\text{ele}} = -\frac{1}{2}\epsilon_0\epsilon_bE_i^2 - E_iP_i \quad (7)$$

where ϵ_0 is the vacuum permittivity and ϵ_b is the background relative dielectric constant.

The simulation size of the (PTO)_{*n*}/(STO)_{*n*} superlattice is 100 × 100 × N_z with a grid spacing of 0.4 nm, corresponding to 40 nm × 40 nm × 0.4 N_z nm in the real space. The (PTO)_{*n*}/(STO)_{*n*} model (n ranges from 3 to 15 unit cells) contains two PTO layers and two STO layers that are alternatively arranged. Because the parameters of scan-date substrates is unknown, we use STO to simulate the substrates.

The periodic boundary condition is applied along the x and y directions. The mixed mechanical boundary condition is applied that the top surface of the film is traction free, while the bottom of the deformable region in the substrate is fixed. A short-circuit electric boundary condition is used where the electric potential at the top film surface and the film/substrate interface is fixed to zero. Inspired by the periodic dipole wave array in the experiment (Fig. 2), with a/c domains whose polarization magnitude is 0.1, \mathbf{P}_s is generated as the initial structure. All material coefficients of PTO and STO are adopted from previous publications (35–37).

We assume that the equilibrium of mechanical stress and electrical field is much faster than the relaxation of domain structures. Thus, for each polarization configurations, the mechanical and electrical equilibrium equations

$$\sigma_{ij,j} = 0 \quad (8)$$

$$D_{i,i} = 0 \quad (9)$$

are solved to obtain the corresponding driving forces.

The evolution of polarization is governed by the time-dependent Ginzburg-Landau equations

$$\frac{\partial P_i(x,t)}{\partial t} = -L \frac{\delta F}{\delta P_i(x,t)} \quad (i = 1, 2, 3) \quad (10)$$

We use the backward Euler method to trace the evolution of polarizations.

SUPPLEMENTARY MATERIALS

Supplementary material for this article is available at <http://advances.sciencemag.org/cgi/content/full/7/28/eabg5503/DC1>

REFERENCES AND NOTES

- K. M. Rabe, C. H. Ahn, J. M. Triscone, *Physics of Ferroelectrics* (Springer, 2007), chap. 5, pp. 177–184.
- Y. L. Tang, Y. L. Zhu, X. L. Ma, A. Y. Borisevich, A. N. Morozovska, E. A. Eliseev, W. Y. Wang, Y. J. Wang, Y. B. Xu, Z. D. Zhang, S. J. Pennycook, Observation of a periodic array of flux-closure quadrants in strained ferroelectric PbTiO₃ films. *Science* **348**, 547–551 (2015).
- Y. Liu, Y.-J. Wang, Y.-L. Zhu, C.-H. Lei, Y.-L. Tang, S. Li, S.-R. Zhang, J. Li, X.-L. Ma, Large scale two-dimensional flux-closure domain arrays in oxide multilayers and their controlled growth. *Nano Lett.* **17**, 7258–7266 (2017).
- A. K. Yadav, C. T. Nelson, S. L. Hsu, Z. Hong, J. D. Clarkson, C. M. Schlepütz, A. R. Damodaran, P. Shafer, E. Arenholz, L. R. Dedon, D. Chen, A. Vishwanath, A. M. Minor, L. Q. Chen, J. F. Scott, L. W. Martin, R. Ramesh, Observation of polar vortices in oxide superlattices. *Nature* **530**, 198–201 (2016).
- Y. Sun, A. Y. Abid, C. Tan, C. Ren, M. Li, N. Li, P. Chen, Y. Li, J. Zhang, X. Zhong, J. Wang, M. Liao, K. Liu, X. Bai, Y. Zhou, D. Yu, P. Gao, Subunit cell-level measurement of polarization in an individual polar vortex. *Sci. Adv.* **5**, eaav4355 (2019).
- M. Guo, C. Guo, J. Han, S. Chen, S. He, T. Tang, Q. Li, J. Strzalka, J. Ma, D. Yi, K. Wang, B. Xu, P. Gao, H. Huang, L.-Q. Chen, S. Zhang, Y.-H. Lin, C.-W. Nan, Y. Shen, Toroidal polar topology in strained ferroelectric polymer. *Science* **371**, 1050–1056 (2021).
- Y.-Y. Tang, Y. Xie, Y. Ai, W.-Q. Liao, P.-F. Li, T. Nakamura, R.-G. Xiong, Organic ferroelectric vortex–antivortex domain structure. *J. Am. Chem. Soc.* **142**, 21932–21937 (2020).
- S. Das, Y. L. Tang, Z. Hong, M. A. P. Gonçalves, M. R. McCarter, C. Klewe, K. X. Nguyen, F. Gómez-Ortiz, P. Shafer, E. Arenholz, V. A. Stoica, S. L. Hsu, B. Wang, C. Ophus, J. F. Liu, C. T. Nelson, S. Saremi, B. Prasad, A. B. Mei, D. G. Schlom, J. Íñiguez, P. García-Fernández, D. A. Müller, L. Q. Chen, J. Junquera, L. W. Martin, R. Ramesh, Observation of room-temperature polar skyrmions. *Nature* **568**, 368–372 (2019).
- Z. Li, Y. Wang, G. Tian, P. Li, L. Zhao, F. Zhang, J. Yao, H. Fan, X. Song, D. Chen, Z. Fan, M. Qin, M. Zeng, Z. Zhang, X. Lu, S. Hu, C. Lei, Q. Zhu, J. Li, X. Gao, J.-M. Liu, High-density array of ferroelectric nanodots with robust and reversibly switchable topological domain states. *Sci. Adv.* **3**, e1700919 (2017).
- W. Yang, G. Tian, Y. Zhang, F. Xue, D. Zheng, L. Zhang, Y. Wang, C. Chen, Z. Fan, Z. Hou, D. Chen, J. Gao, M. Zeng, M. Qin, L.-Q. Chen, X. Gao, J.-M. Liu, Quasi-one-dimensional metallic conduction channels in exotic ferroelectric topological defects. *Nat. Commun.* **12**, 1306 (2021).
- Y. J. Wang, Y. P. Feng, Y. L. Zhu, Y. L. Tang, L. X. Yang, M. J. Zou, W. R. Geng, M. J. Han, X. W. Guo, B. Wu, X. L. Ma, Polar meron lattice in strained oxide ferroelectrics. *Nat. Mater.* **19**, 881–886 (2020).
- A. Du, G. Z. Wei, Spin-wave theory on quasi-one-dimensional heisenberg antiferromagnets. *Phys. Stat. Sol. B* **191**, 495–501 (1995).
- C. Herring, C. Kittel, On the theory of spin waves in ferromagnetic media. *Phys. Rev.* **81**, 869–880 (1951).
- K. S. Bedell, H. P. Dahal, Spin waves in quasiequilibrium spin systems. *Phys. Rev. Lett.* **97**, 047204 (2006).
- M. Dixon, F. E. Hoare, T. M. Holden, The specific heat of magnetite. *Phys. Lett.* **14**, 184–185 (1965).
- W. N. Lawless, Specific heats of paraelectrics, ferroelectrics, and antiferroelectrics at low temperatures. *Phys. Rev. B* **14**, 134–143 (1976).
- W. N. Lawless, A. J. Morrow, Further studies of the T^{3/2} specific heat term in ferroelectrics at low temperatures. *Ferroelectrics* **15**, 167–171 (1977).
- W. N. Lawless, T^{3/2} contribution to the specific heat of ferroelectrics at low temperatures. *Phys. Rev. Lett.* **36**, 478–479 (1976).
- W. N. Lawless, Origin of the T^{3/2} specific-heat term in triglycine sulfate at low temperatures. *Phys. Rev. B* **23**, 2421–2424 (1981).
- M. C. Foote, A. C. Anderson, Low-temperature specific heats of BaTiO₃ and KH₂PO₄. *Ferroelectrics* **62**, 11–15 (1985).
- W. N. Lawless, T. D. Lawless, Specific heat studies of small KDP crystals at low temperatures. *Ferroelectrics* **45**, 149–155 (1982).
- W. N. Lawless, Specific heat properties of KH₂PO₄. *Ferroelectrics* **71**, 149–160 (1987).
- W. N. Lawless, Low temperature specific heats of some PLZT ceramics. *Ferroelectrics* **15**, 61–67 (1977).
- J. A. Gonzalo, Ferroelectric dipole waves. *Ferroelectrics* **20**, 159–161 (1978).
- J. A. Gonzalo, Ferroelectric elementary excitations at low temperatures: Dipole waves. *J. Phys. C Solid State Phys.* **20**, 3985–3992 (1987).
- H. Sugimoto, S. Ikeda, Electric dipole waves and vibration motion of protons in hydrogen-bonded crystalline KH₂PO₄ at low temperatures. *J. Phys. Condes. Matter* **6**, 5561–5575 (1994).
- D. Sichuga, L. Bellaiche, Epitaxial Pb(Zr, Ti)O₃ ultrathin films under open-circuit electrical boundary conditions. *Phys. Rev. Lett.* **106**, 196102 (2011).
- A. R. Damodaran, J. D. Clarkson, Z. Hong, H. Liu, A. K. Yadav, C. T. Nelson, S. L. Hsu, M. R. McCarter, K. D. Park, V. Kravtsov, A. Farhan, Y. Dong, Z. Cai, H. Zhou, P. Aguado-Puente, P. García-Fernández, J. Íñiguez, J. Junquera, A. Scholl, M. B. Raschke, L. Q. Chen, D. Fong, R. Ramesh, L. W. Martin, Phase coexistence and electric-field control of toroidal order in oxide superlattices. *Nat. Mater.* **16**, 1003–1009 (2017).
- K. Du, M. Zhang, C. Dai, Z. N. Zhou, Y. W. Xie, Z. H. Ren, H. Tian, L. Q. Chen, G. V. Tendeloo, Z. Zhang, Manipulating topological transformations of polar structures through real-time observation of the dynamic polarization evolution. *Nat. Commun.* **10**, 4864 (2019).
- L. Lu, Y. Nahas, M. Liu, H. Du, Z. Jiang, S. Ren, D. Wang, L. Jin, S. Prokhorenko, C.-L. Jia, L. Bellaiche, Topological defects with distinct dipole configurations in PbTiO₃/SrTiO₃ multilayer films. *Phys. Rev. Lett.* **120**, 177601 (2018).
- J. Ma, Y. Zhu, Y. Tang, M. Han, Y. Wang, N. Zhang, M. Zou, Y. Feng, W. Geng, X. Ma, Modulation of charged a₁/a₂ domains and piezoresponses of tensile strained PbTiO₃ films by the cooling rate. *RSC Adv.* **9**, 13981–13990 (2019).
- V. A. Stoica, N. Laanait, C. Dai, Z. Hong, Y. Yuan, Z. Zhang, S. Lei, M. R. McCarter, A. Yadav, A. R. Damodaran, S. Das, G. A. Stone, J. Karapetrova, D. A. Walko, X. Zhang, L. W. Martin, R. Ramesh, L. Q. Chen, H. Wen, V. Gopalan, J. W. Freeland, Optical creation of a supercrystal with three-dimensional nanoscale periodicity. *Nat. Mater.* **18**, 377–383 (2019).
- S. M. Anthony, S. Granick, Image analysis with rapid and accurate two-dimensional gaussian fitting. *Langmuir* **25**, 8152–8160 (2009).
- C. L. Jia, V. Nagarajan, J. Q. He, L. Houben, T. Zhao, R. Ramesh, K. Urban, R. Waser, Unit-cell scale mapping of ferroelectricity and tetragonality in epitaxial ultrathin ferroelectric films. *Nat. Mater.* **6**, 64–69 (2007).
- Y. L. Li, S. Y. Hu, Z. K. Liu, L. Q. Chen, Effect of substrate constraint on the stability and evolution of ferroelectric domain structures in thin films. *Acta Mater.* **50**, 395–411 (2002).
- Y. L. Li, S. Y. Hu, D. Tenne, A. Soukiasian, D. G. Schlom, X. X. Xi, K. J. Choi, C. B. Eom, A. Saxena, T. Lookman, Q. X. Jia, L. Q. Chen, Prediction of ferroelectricity in BaTiO₃/SrTiO₃ superlattices with domains. *Appl. Phys. Lett.* **91**, 112914 (2007).
- Y.-J. Wang, J. Li, Y.-L. Zhu, X.-L. Ma, Phase-field modeling and electronic structural analysis of flexoelectric effect at 180° domain walls in ferroelectric PbTiO₃. *J. Appl. Phys.* **122**, 224101 (2017).
- R. Uecker, B. Velickov, D. Klimm, R. Bertram, M. Bernhagen, M. Rabe, M. Albrecht, R. Fornari, D. G. Schlom, Properties of rare-earth scandate single crystals (Re=Nd–Dy). *J. Cryst. Growth* **310**, 2649–2658 (2008).
- B. Velickov, V. Kahlenberg, R. Bertram, M. Bernhagen, Crystal chemistry of GdScO₃, DyScO₃, SmScO₃, and NdScO₃. *Z. Kristallogr.* **222**, 466–473 (2007).

Acknowledgments: We are grateful to L.-X. Yang of this laboratory for technical support on the Titan platform of G² 60-300 aberration-corrected STEM. **Funding:** This work is supported by the National Natural Science Foundation of China (nos. 51971223, 51671194, and 51922100), the Key Research Program of Frontier Sciences CAS (QYZDJ-SSW-JSC010), and the Shenyang National Laboratory for Materials Science (L2019R06, L2019R08, L2019F01, and L2019F13). Y.-L.T. acknowledges the Scientific Instrument Developing Project of CAS (YJKYYQ20200066) and the Youth Innovation Promotion Association of CAS (Y202048). Y.-J.W. acknowledges the Youth Innovation Promotion Association CAS (no. 2021187). **Author contributions:** X.-L.M. and Y.-L.Z. conceived the project of interfacial characterization in oxides by using aberration-corrected STEM. F.-H.G., Y.-L.T., Y.-L.Z., and X.-L.M. designed the experiments. F.-H.G. and Y.-L.T. performed the thin-film growth and STEM observations. H.Z. and Y.-J.W. carried out the phase-field calculations. Y.-T.C., Y.-P.F., M.-J.Z., B.W., W.-R.G., and Y.-J.W. participated in the thin-film growth and STEM imaging. All authors contributed to the discussions and manuscript preparation. **Competing interests:** The authors declare that they have no competing interests. **Data and materials availability:** All data needed to evaluate the conclusions in the paper are present in the paper and/or the Supplementary Materials. Additional data related to this paper may be requested from the authors.

Submitted 13 January 2021

Accepted 27 May 2021

Published 9 July 2021

10.1126/sciadv.abg5503

Citation: F.-H. Gong, Y.-L. Tang, Y.-L. Zhu, H. Zhang, Y.-J. Wang, Y.-T. Chen, Y.-P. Feng, M.-J. Zou, B. Wu, W.-R. Geng, Y. Cao, X.-L. Ma, Atomic mapping of periodic dipole waves in ferroelectric oxide. *Sci. Adv.* **7**, eabg5503 (2021).

Atomic mapping of periodic dipole waves in ferroelectric oxide

Feng-Hui Gong, Yun-Long Tang, Yin-Lian Zhu, Heng Zhang, Yu-Jia Wang, Yu-Ting Chen, Yan-Peng Feng, Min-Jie Zou, Bo Wu, Wan-Rong Geng, Yi Cao and Xiu-Liang Ma

Sci Adv 7 (28), eabg5503.
DOI: 10.1126/sciadv.abg5503

ARTICLE TOOLS	http://advances.sciencemag.org/content/7/28/eabg5503
SUPPLEMENTARY MATERIALS	http://advances.sciencemag.org/content/suppl/2021/07/02/7.28.eabg5503.DC1
REFERENCES	This article cites 38 articles, 4 of which you can access for free http://advances.sciencemag.org/content/7/28/eabg5503#BIBL
PERMISSIONS	http://www.sciencemag.org/help/reprints-and-permissions

Use of this article is subject to the [Terms of Service](#)

Science Advances (ISSN 2375-2548) is published by the American Association for the Advancement of Science, 1200 New York Avenue NW, Washington, DC 20005. The title *Science Advances* is a registered trademark of AAAS.

Copyright © 2021 The Authors, some rights reserved; exclusive licensee American Association for the Advancement of Science. No claim to original U.S. Government Works. Distributed under a Creative Commons Attribution NonCommercial License 4.0 (CC BY-NC).